CrossMark

Controlled hydrothermal synthesis, excellent optical and magnetic properties of CeO_2 nanocubes

Lei Qin[1] · Xiaofei Niu[1]

Abstract The CeO_2 nanocubes with rough surface have been successfully synthesized by a facile hydrothermal technique. The reaction temperature was systematically investigated. X-ray diffractometer, scanning electron microscope, transmission electron microscope, X-ray photoelectron spectroscopy, Raman scattering, ultraviolet–visible and Photoluminescence spectra, and magnetization hysteresis (*M–H*) curves were employed to characterize the samples. The results showed that all the CeO_2 nanocubes owned a fluorite cubic structure and there are Ce^{3+} ions and oxygen vacancies in surface of samples. Although the morphology had a slight difference for the samples synthesized at different temperature and the average edge length of the nanocubes increased from ~ 150 to ~ 250 nm, then to ~ 350 nm with the enhancement of temperature, the cube-like morphology remained unchanged. The synthesized CeO_2 samples show excellent room temperature optical properties. The *M–H* curves of CeO_2 nano-octahedrons exhibit excellent room-temperature ferromagnetism, which is likely attributed to the effects of the different morphology of samples, Ce^{3+} ions and oxygen vacancies.

1 Introduction

In recent years, there has been increasing interest in the controlled synthesis of higher ordered inorganic crystals with specific dimensions and well-defined shapes because of the unique shape-dependent materials properties, which would result in a wide range of electrical, optical, or magnetic properties and open a new domain of theoretical and technological interest [1–4]. Therefore, considerable efforts have been focused on the fabrication of nanomaterials with various morphology structures owning to stimulated by the fantastic and remarkable properties.

As one of the most important rare earth oxides, CeO_2 with remarkable properties due to its abundant oxygen vacancy defects, high oxygen storage capacity and ability to uptake and release oxygen via the transformation between Ce^{3+} and Ce^{4+}, has been the subject of intense interest and widely used in oxygen storage capacity [5], catalyst [6], fuel cells [7], gas sensors [8], dye removal treatments [9], and optical properties [10] and magnetic properties [11]. Recent advances in the morphology-controlled synthesis of the nanomaterials offer new opportunities of developing novel CeO_2 functional materials with desired structural properties. CeO_2 with various morphologies such as nanospheres [12], nanoflowers [13], nanoplates [14], nanoshuttles [15], nano-octahedrons [16], nanowires [17], nanotubes [18], nanorods [19] and other morphologies [3, 4] has been synthesized in recent years. Although significant progress in the synthesis approaches for CeO_2 with various morphologies has been achieved, the higher synthesis cost, larger energy consumption and more complicated manufacturing procedures are usually unavoidable. Among these methods, the hydrothermal synthesis technique has been regarded as one of the most effective and attractive routes, due to its own merits of high powder reactivity, versatile shape control, and a large-scale industrialization. As is well-known, it is difficult to synthesize materials with nanostructures in solution-phase, especially materials with a face-centered cubic structure (for example CeO_2), since there is no intrinsic driving force to form an anisotropic morphology.

✉ Lei Qin
  tougao1216@126.com

[1] Anhui Key Laboratory of Spintronics and Nanomaterials Research, Suzhou University, Suzhou 234000, China

In this paper, we reported facile, smart and low-cost hydrothermal route to synthesize CeO_2 nanocubes with a rough surface using $CeCl_3 \cdot 7H_2O$ as cerium source, $NH_4\text{HCO}_3$ as precipitator. The morphology of CeO_2 can be controlled by adjusting the reaction temperature. The CeO_2 nanocubes show excellent room temperature optical and magnetic properties. Our method is an effective approach to controlling CeO_2 morphology and size which may be extended to synthesis of other nanomaterials.

2 Experimental

2.1 Material preparation

Up to now, many studies on hydrothermal syntheses of CeO_2 have been reported [2–4]. All the reagents were of analytical grade purity and used as received without further purification before the synthesized process. In a typical synthesis procedure, 4 mmol cerium chloride heptahydrate $(CeCl_3 \cdot 7H_2O)$ and 50 mmol ammonium bicarbonate $(NH_4\text{HCO}_3)$ were dissolved in 10 and 25 mL deionized water, respectively. After continuous stirring for 1 h, 25 mL $NH_4\text{HCO}_3$ aqueous solution were rapidly poured into 10 mL $CeCl_3 \cdot 7H_2O$ aqueous solution under continuous stirring. Continuous stirring for a long time before the white suspending solution was transferred into a 50 mL Teflon-lined autoclave and heated at 100, 120 and 160 °C for 48 h, followed by natural cooling to room temperature. The fresh precipitates were washed with distilled water and ethanol three times in turn, and then dried at 80 °C for 12 h. The light yellow CeO_2 were obtained after the resultant powders were calcined at 500 °C for 4 h in air. The products of others were obtained through a similar procedure except using the amount of ethanediamine 1 mL instead of 0 mL.

2.2 Characterization

Crystal structures of the samples were characterized by X-ray diffractometer (XRD, XD-3) with Cu Kα radiation ($\lambda = 0.154$ nm). Morphologies and sizes of synthesized nanoparticles were studied by scanning electron microscope (SEM, S-4800, Japan) and transmission electron microscope (TEM, JEM-2100, Japan). The chemical state was analyzed by X-ray photoelectron spectroscopy (XPS, ESCALAB 250 US Thermo Electron Co). The Raman spectra were carried out by a Raman spectrometer system (inVia-Reflex) using a laser with 532 nm excitation. The ultraviolet–visible (UV–Vis) diffuse reflectance spectra were carried out using an ultraviolet–visible-near infrared spectrophotometer (U-4100). Photoluminescent (PL) emission spectra were recorded on a fluorescence

spectrophotometer (Hitachi F-4500) using excitation light of 330 nm. The *M–H* curves were measured at room temperature by a vibrating sample magnetometer (BHV-55).

3 Results and discussion

3.1 XRD characterization

X-ray diffractometer (XRD) analysis was carried out to investigate the crystal phase and purity of the samples. Figure 1 shows the XRD patterns of the products obtained at 100, 120, 160 °C for 48 h. All the detectable peaks can be well-indexed to a pure cubic structure of CeO_2, which is in good agreement with the JCPDS file for CeO_2 ($Fm\overline{3}m$, JCPDS No. 43-1002). It is noteworthy that no diffraction peaks from other species can be detected by XRD patterns, indicating a high purity of the final products and the hydrothermal reaction temperature has no effect on CeO_2 crystalline phase purity. Moreover, the sharp diffraction peaks from all samples suggest a good crystallinity of the obtained CeO_2 nanocrystals. The relative intensity between characteristic peaks at about 28.58, 33.10 47.36 and 56.29 (2θ) does not change clearly, which assigned to the crystal planes (111), (200), (220) and (311) respectively, suggesting that there is no preferred orientation or orientation crystal growth.

3.2 SEM and TEM characterization

The morphology and size of CeO_2 samples synthesized at different temperature were investigated by SEM and TEM. As shown in Fig. 2a, the uniform cubic particles have an average edge length of about 150 nm. In the inset image of
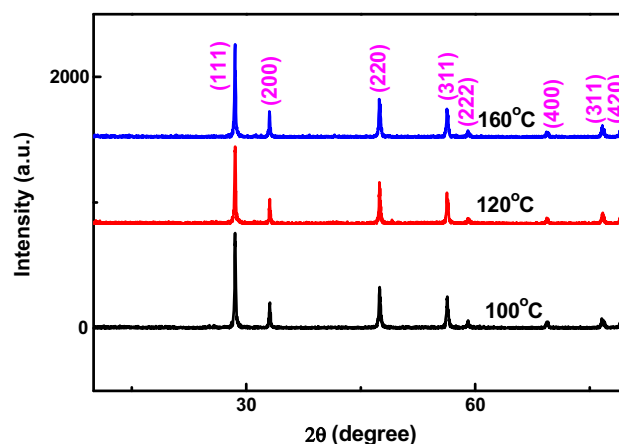

Fig. 1 XRD patterns of products synthesized at 100, 120, and 160 °C for 48 h
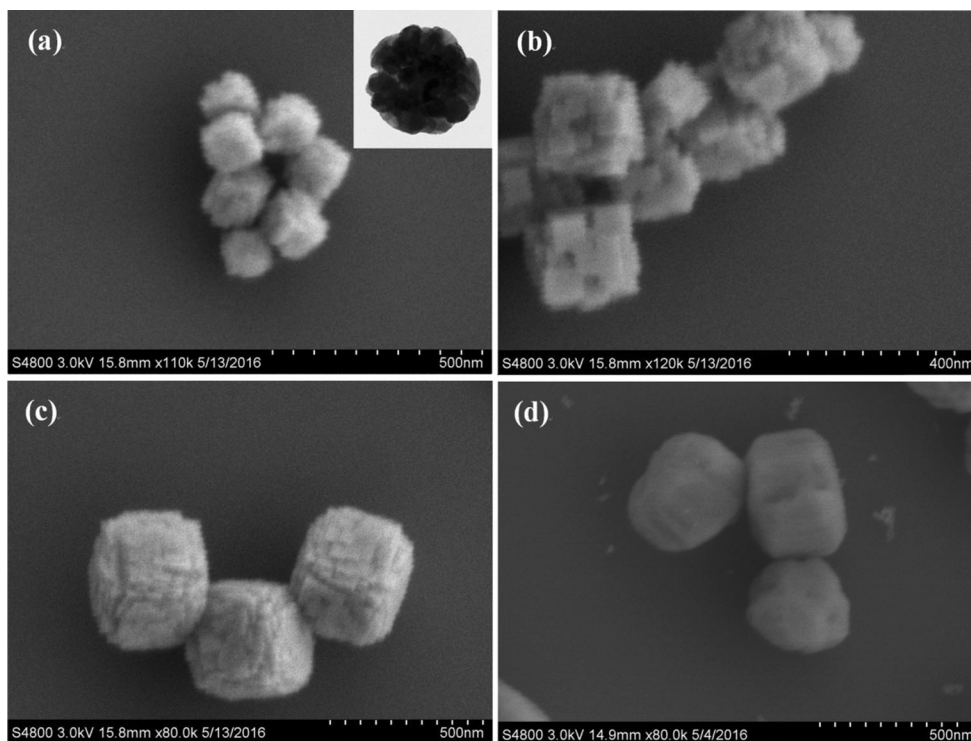
Fig. 2 SEM images of products synthesized at **a** 100 °C, **b** 120 °C, **c** 160 °C for 48 h, **d** the products synthesized at 160 °C for 48 h doped 0 mL ethylenediamine

Fig. 2a, one can note that the nanocubes have a loosened body and crude surface which is covered by wrinkles completely. These wrinkled surfaces result in a high specific surface area for the nanocubes, which would be beneficial for enhancing their physical and chemical properties. Increasing the reaction temperature to 120 °C, as shown in Fig. 2b, the average edge length of the nano-cubes increased from ~ 150 to ~ 250 nm, while overall outline of the nanocubes remained unchanged. Further-more, the nanocubes not have a loosened body and crude surface, but a cube-like structure composed of numerous small nanocubes as the building block with an average edge length of about 60 nm, which orderly stack together to form a cube-like structure with many pores. When the reaction temperature is up to 160 °C, the average edge length of the nanocubes increased from ~ 250 to ~ 350 nm, while the cube-like morphology and crude surface remained unchanged, as shown in Fig. 2c. When 1 mL ethanediamine was added into solution and reaction temperature was kept at 160 °C, the spherical particles with a smooth but irregular surface while the size remained unchanged, as shown in Fig. 2d.

3.3 Composition and chemical state

To further characterize the product, XPS analysis was carried out to investigate the surface composition and

chemical state of the CeO_2 nanocubes synthesized at 160 °C for 48 h. The Ce 3d spectra and corresponding peak fitted deconvolutions are given in Fig. 3a. Eight peaks associated with the 3d electrons of Ce correspond to four pairs of spin–orbit doublets [20]. From Fig. 3a, it can be seen that six Ce 3d BE peaks, at 916.51, 908.20, 899.44, 898.22, 888.29 and 882.05 eV are attributed to $3d_{3/2}$ and $3d_{5/2}$ for Ce^{4+} final states [21], while two weak peaks at 901.24 and 883.21 eV are the present for $3d_{3/2}$ and $3d_{5/2}$ for Ce^{3+} 3d final states [22]. This result indicates that the main valence of cerium in the sample was +4, and a small amount of Ce^{3+} distributes around oxygen vacancies on the CeO_2 surfaces [23], regardless of the valence of the starting cerium salts. Figure 3b shows The O1s spectra of the CeO_2 nanocubes. It can be seen that three BE peaks at binding energy 528.82, 529.81 and 531.11 eV can be attributed to lattice oxygen ions in CeO_2, absorbed oxygen and lattice oxygen ions in Ce_2O_3 [24–26], respectively.

3.4 Optical properties

To understand the defect induced changes in the local structure of CeO_2 nanocrystals and to characterize oxygen vacancies, a very facile and nonvolatile technique, Raman spectroscopy was carried out. Figure 4 shows the recorded Raman spectra of the as-obtained products under different hydrothermal temperature. As we have seen from Fig. 4,
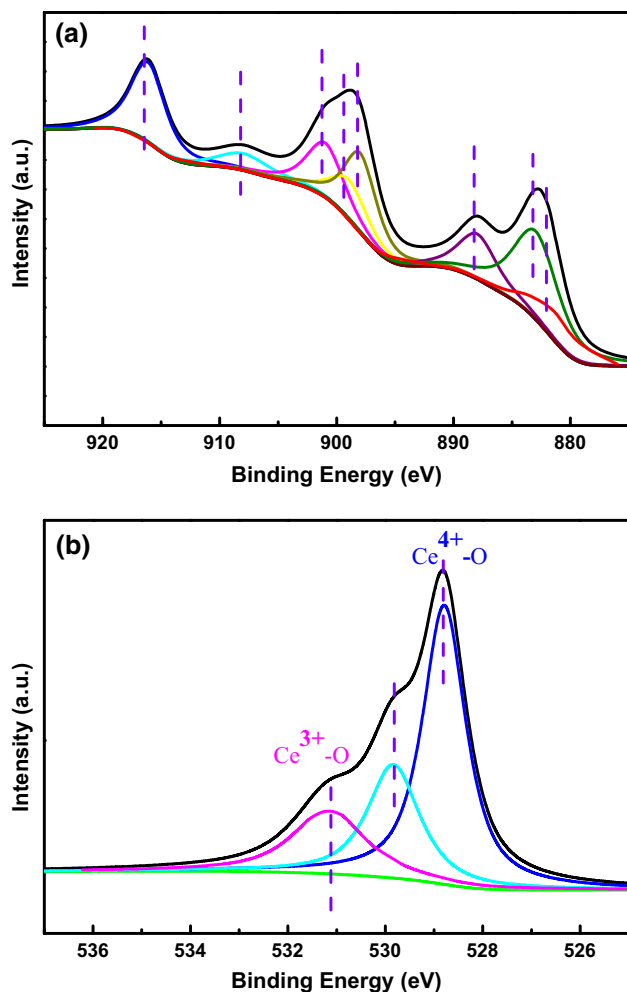
Fig. 3 XPS cores level spectra of Ce3d (**a**) and O1s (**b**) of CeO$_2$ nanocubes obtained at 160 °C for 48 h

Fig. 4 Raman spectra of CeO$_2$ nanocubes obtained at 100, 120 and 160 °C for 48 h, respectively

one strong scattering peak observed at about 462 cm^{-1}, corresponding to the triply degenerate F$_{2g}$ mode of the fluorite crystal structure of CeO$_2$ and it can be considered as the symmetric stretching mode of oxygen atoms around cerium ions, and the molecule retains its tetrahedral symmetry throughout [27]. Because only the O atoms move, the vibrational mode is nearly independent of the cation mass [28]. So, the only peak allowed in first order should be very sensitive to any disorder in the oxygen sublattice resulting from thermal, doping, or grain size [29]. However, it is well known that bulk CeO$_2$ has a main peak at 465 cm^{-1}, but under the circumstances, the main peak shifts toward lower wavenumber and becomes more asymmetric, several factors, such as phonon confinement, increased lattice strain, nonuniform strain and variations in phonon relaxation may account for the changes [30]. It is likely that Ce^{3+} ions and oxygen vacancies in the samples are responsible for the changes in the Raman scattering as supported by the XPS and PL data. In addition, the low
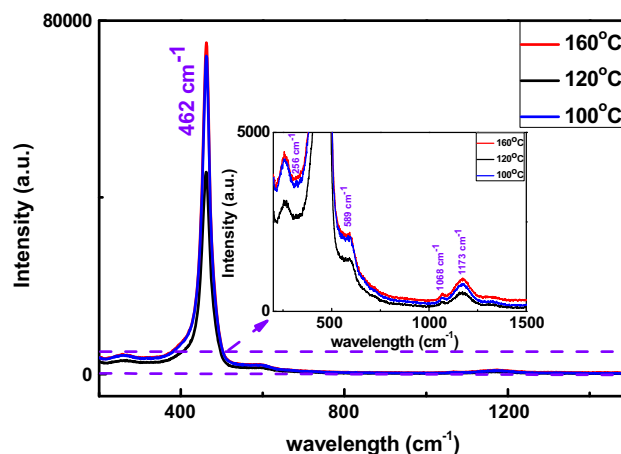
intense peaks at 256 cm^{-1} may be assigned to the disorder in the system [31], while the peaks at 589 cm^{-1} can be attributed to defect spaces which include oxygen vacancies [32]. The samples obtained at 160 °C have a highest intensity at 589 cm^{-1}, which may be due to the formation of more oxygen vacancies. In this respect, as far as we know that the introduction of oxygen vacancies or increasing the concentration at the surface of CeO$_2$ samples can inhibit the recombination of electron–hole pairs to improve their performance as efficient photocatalysts [25]. In fact, it makes no any sense to assign the broad and asymmetrical peak at about 1068 cm^{-1} to a single critical point phonon overtone. Finally, the second-order feature at 1173 cm^{-1} is ascribed to the second-order Raman mode of surface superoxide species (O_2^-), and has little additional contributions from F$_{2g}$ symmetry [33].

The UV–Vis diffuse reflectance spectra of samples prepared within different reaction temperatures are shown in Fig. 5a. All the samples showed strong absorption below 400 nm corresponding to the fluorite cubic structure of CeO$_2$, which originates from the charge-transfer transition between the O^{2-} (2p) and Ce^{4+} (4f) orbit in CeO$_2$ [3]. The nanocubes synthesized at 160 °C were observed to have higher absorptions of the blue and UV lights than others, allowing it to be used as a better UV blocker. According to previous reports [34] that not all cerium ions show Ce^{4+} chemical valence in the lattice and small cerium ions show Ce^{3+} tervalence. So as to maintain the particles in an electrically neutral state, the lattice oxygen would escape from the structure and finally result in the formation of intrinsic oxygen vacancies. The absorption band of the nanocubes synthesized at 160 °C extended to longer wavelength, indicating the Ce^{3+} supply lower unoccupied orbits than Ce 4f, thus the transition from O 2p to the unoccupied orbits needs lower energy. So, we can conclude
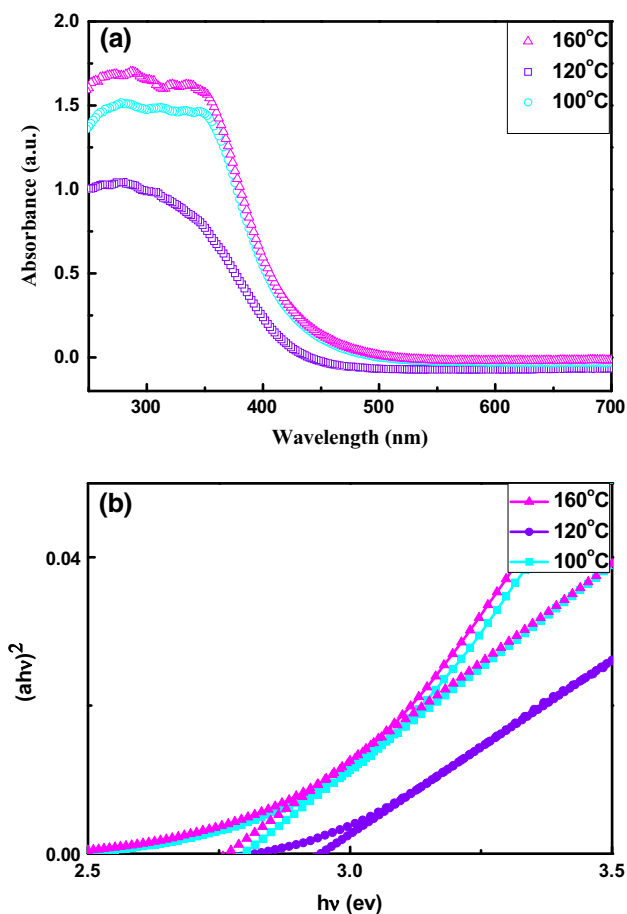
Fig. 5 a UV–Vis absorption spectra, **b** plots of $(\alpha h v)^2$ as function of energy of CeO$_2$ nanocubes obtained at 100, 120 and 160 °C for 48 h, respectively

that the nanocubes synthesized at 160 °C have more intrinsic defects (oxygen vacancies) [3]. According to the data of the absorption spectra, the optical band gaps (E_g) of CeO$_2$ nanoparticles can be estimated by using the following equation [35]: $(\alpha h v)^n = B(h v - E_g)$. Where α is the absorption coefficient, B is a constant relative to the material, $h v$ is the photon energy, and n is 2 for a direct transition. The plots of $(\alpha h v)^2$ versus photon energy for all the CeO$_2$ samples are shown in Fig. 5b. As a result, the values of band gap energy are 2.79, 2.94 and 2.77 eV, for the CeO$_2$ samples synthesized within 100, 120 and 160 °C, respectively, Which is smaller than the value of the traditional bulk CeO$_2$ ($E_g = 3.20$ eV). According to the literature, a red-shifting phenomenon could be attributed to electron–phonon coupling [36] and the shape of the material [3]. However, a complementary viewpoint about it is provided by our work. It is well-known that ceria possesses intrinsic defect (Ce^{3+} and O vacancy concentration) in the fluorite structure, which generally introduces intermediate energy levels, thus resulting in a decrease in the

band gap. Therefore, decrease in band gap indicates more Ce^{3+} ions and O vacancies in the obtained CeO$_2$, which is in agreement with the PL and Raman spectra analyses.

The photoluminescence (PL) performance of CeO$_2$ is attributed to the strong light absorption through the charge transfer between O^{2-} and Ce^{4+}. As we all know that CeO$_2$ is a wide band semiconductor, whose Ce 4f energy levels is localized at the forbidden gap and lie ~ 3 eV above the valence band (O 2p). When the electronic transition takes place, the excited electrons will populate Ce 4f as well as vacant spaces of oxygen defects. The defects energy levels of CeO$_2$ localized between the Ce 4f band and O 2p band can lead to broad emission bands. Since every atoms, ions or each kind of defects do not emit the same spectra [37]. Figure 6 shows the PL spectra of all CeO$_2$ nanocubes measured at room temperature at an excitation wavelength of 330 nm. All samples have almost the same emission peaks and show a strong PL emission single at 473 nm, the weak emission band centred on 425 and 532 nm are also observed. On the other hand, their PL intensities are slightly different from each other and the peak intensity decreases with the increase of reaction temperature and then increases, which can be reasonably explained for that different morphology and size of the particles may influence the carriers excited from the valence band to the conduction band and then relax their energy on the crystal surface and lead to variations of luminescence properties [21]. Up to now, a number of studies on PL of CeO$_2$ have been reported. Maensiri et al. [38] observed a wide PL emission band from 390 to 550 nm in CeO$_2$ nanoparticles, and they believed that the surface defects are responsible for the broad emission. Jiang et al. [39] observed two subpeaks at 452 and 470 nm, which exist obvious inversions in the relative intensity in the two PL spectra at two
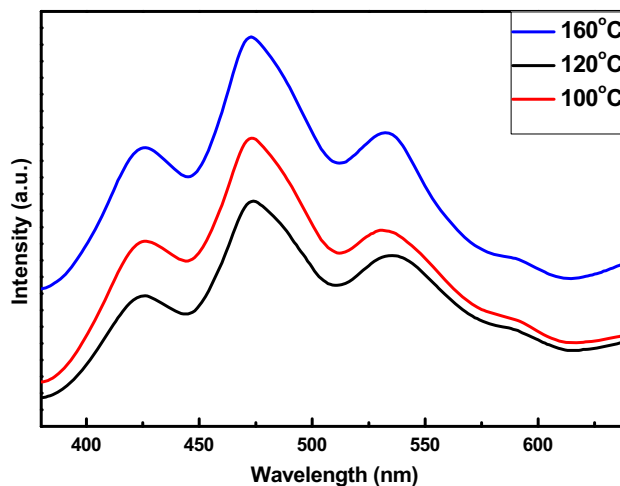

Fig. 6 Photoluminescence spectra of CeO$_2$ nanocubes obtained at 100, 120 and 160 °C for 48 h, respectively

different excitation wavelengths (290 and 340 nm). The two peaks at 415 and 435 nm can be found from the flowerlike CeO_2 [40], while three emission peaks located at 370, 414 and 468 nm have been reported for the rod-like CeO_2 [41]. The weak emission band centered on 540 and 564 nm may be induced by the oxygen vacancies in the pole-like nanostructures [2]. The investigation showed that the emission bands ranging from 400 to 500 nm for CeO_2 sample are attributed to the hopping from different defect levels to valence band, and can be partly certificated by comparing the relationship of peak intensity and band gap [40, 42]. The weak emission band centered on 532 nm may be attributed to the oxygen vacancies in the crystal with defect energy levels below the Ce 4f band [22].

The magnetic properties of CeO_2 nanocubes were characterized by measuring the field dependence of magnetization at room temperature. Figure 7a shows the M–H curves of all the CeO_2 nanocubes at room temperature and Fig. 7b is the magnetization of the central part. As we
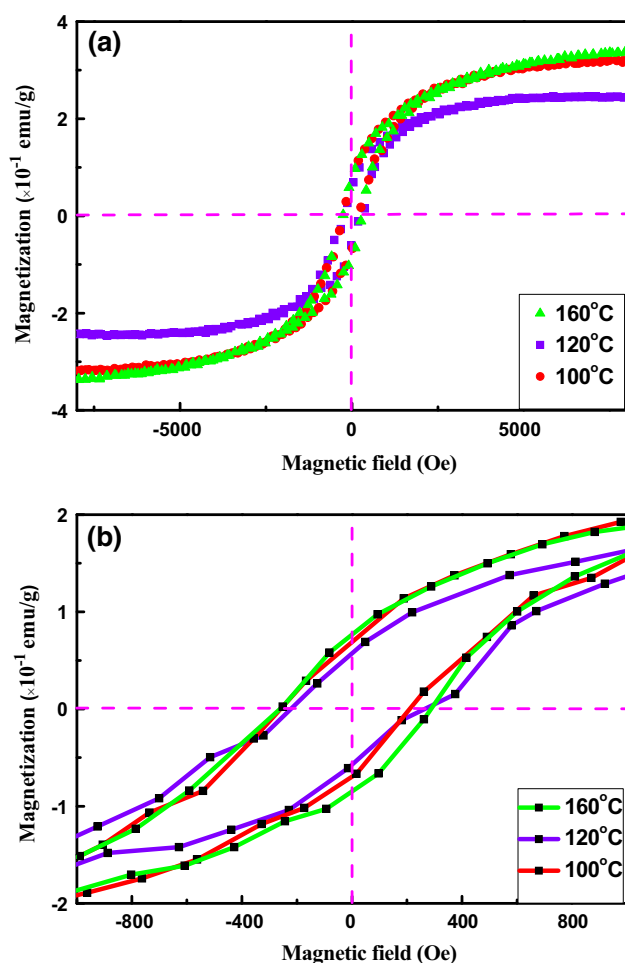
Table 1 The parameters of M_s, M_r and H_c for CeO_2 nanocubes obtained at 100, 120 and 160 °C for 48 h, respectively

Temperature	M_s (emu/g)	M_r (emu/g)	H_c (Oe)
100 °C	0.31	0.69	285
120 °C	0.24	0.55	249
160 °C	0.35	0.80	295

can see that all samples exhibit a very well defined hysteresis loop and the nanocubes synthesized at 160 °C have a higher coercivity than that of others. The parameters of M_s, M_r and H_c for all CeO_2 cube-like samples are shown in Table 1. All the parameters decrease with the enhancement of reaction temperature, and then increase. Interestingly, these values of M_s are larger than those previous reports in which the pure CeO_2 [43, 44] and CeO_2 nanoparticles were doped with magnetic element, such as Ni, Co and Cu [45–47]. From those reports, it can be concluded that magnetic not only from doped elements, but a part of CeO_2 itself becomes magnetic, although bulk CeO_2 with a face-centered cubic structure is paramagnetic. Firstly, according to the results of XPS and Raman analyses, it can be concluded that Ce^{3+} and oxygen vacancy existed in the surface of CeO_2 samples. When the valence of Ce changes from +4 to +3, the electron orbits (Ce^{4+}–O^{2-}–Ce^{3+}) are no longer symmetrical and an uncoupled spins in the Ce 4f orbit are generated. Therefore, the room-temperature ferromagnetism (RTFM) might consequently arise from a nearest-neighbor interaction: double exchange (Ce^{4+}–O^{2-}–Ce^{3+}) [48]. Secondly, from experimental and theoretical studies, oxygen vacancies were supposed to give rise to the RTFM. In addition, Bernardi et al. [49] has confirmed that the presence of substantial oxygen vacancies would lead to magnetic order. Wang et al. [50] also believed that the FM of CeO_2 samples is related to the concentration of Ce^{3+} and oxygen deficiencies. From the above, the RTFM of the CeO_2 samples may be ascribed to the effects of the different morphology of samples, Ce^{3+} ions and oxygen vacancies.

Fig. 7 M–H curves of CeO_2 nanocubes obtained at 100, 120 and 160 °C for 48 h, respectively and the *inset* figure presents the spectra in a suitable scale

4 Conclusions

In summary, we have demonstrated a facile approach to the synthesis of CeO_2 with cube-like nanostructures only using simple starting materials in a hydrothermal system. Although the CeO_2 nanocubes obtained at different temperature have similar morphology, the higher the temperature, the more conducive to increase the size of nanocubes. It was found that the nanocubes have a fluorite cubic structure and and there are Ce^{3+} ions and oxygen vacancies existing in surface of samples. Although the

visible luminescence exhibits similar emission peaks, the emission intensity is diverse from each other and the emission intensity of the samples obtained at 160 °C is highest. The ultraviolet–visible (UV–Vis) absorption spectra of the all CeO_2 samples show the excellent ultraviolet shelter ability and red-shift compared with the bulk CeO_2. All the nanocubes exhibit excellent behavior of ferromagnetism, especially the samples obtained at 160 °C, which may be attributed to the effects of the change of morphology, Ce^{3+} ions and oxygen vacancies. The controllable morphology, excellent optical properties and RTFM should make the CeO_2 nanocubes as an excellent candidate for nano particles application in related areas. It is anticipated that this work can shed new light on the synthesis of nanomaterials.

References

1. J. Li, H.Q. Fan, X.H. Jia, J. Phys. Chem. C **114**, 14684 (2010)
2. L.N. Wang, F.M. Meng, K.K. Li, F. Lu, Appl. Surf. Sci. **286**, 269 (2013)
3. B. Xu, Q.T. Zhang, S.S. Yuan, M. Zhang, T. Ohno, Chem. Eng. J. **260**, 126 (2015)
4. R.C. Rao, M. Yang, C.S. Li, H.Z. Dong, S. Fang, A.M. Zhang, J. Mater. Chem. A **3**, 782 (2015)
5. J. Zhang, H. Kumagai, K. Yamamura, S. Ohara, S. Takami, A. Morikawa, H. Shinjoh, K. Kaneko, T. Adschiri, A. Suda, Nano Lett. **11**, 361 (2011)
6. C.T. Campbell, C.H.F. Peden, Science **309**, 713 (2005)
7. P. Bera, A. Gayen, M.S. Hegde, N.P. Lalla, L. Spadaro, F. Frusteri, F. Arena, J. Phys. Chem. B **107**, 6122 (2003)
8. N. Izu, T. Itoh, M. Nishibori, I. Matsubara, W. Shin, Sens. Actuat. B Chem. **171**, 350 (2012)
9. H. Li, G.F. Wang, F. Zhang, Y. Cai, Y.D. Wang, I. Djerd, RSC Adv. **2**, 12413 (2012)
10. Z.L. Wang, Z.W. Quan, J. Lin, Inorg. Chem. **46**, 5237 (2007)
11. R.K. Singhal, S. Kumar, A. Samariya, M. Dhawan, S.C. Sharma, Y.T. Xing, Mater. Chem. Phys. **132**, 534 (2012)
12. Z. Yang, D. Han, D. Ma, H. Liang, L. Liu, Y. Yang, Cryst. Growth Des. **10**, 291 (2010)
13. J. Wei, Z. Yang, H. Yang, T. Sun, Y. Yang, CrystEngComm **13**, 4950 (2011)
14. H. Imagawa, S.H. Sun, J. Phys. Chem. C **116**, 2761 (2012)
15. Z. Guo, F. Du, G. Li, Z. Cui, Cryst. Growth Des. **8**, 2674 (2008)
16. X.H. Lu, X. Huang, S.L. Xie, D.Z. Zheng, Z.Q. Liu, C.L. Liang, Y.X. Tong, Langmuir **26**, 7569 (2010)
17. X.H. Lu, D.Z. Zheng, J.Y. Gan, Z.Q. Liu, C.L. Liang, P. Liu, Y.X. Tong, J. Mater. Chem. **20**, 7118 (2010)
18. G.Z. Chen, C.X. Xu, X.Y. Song, W. Zhao, Y. Ding, S.X. Sun, Inorg. Chem. **47**, 723 (2008)
19. K.B. Zhou, X. Wang, X.M. Sun, Q. Peng, Y.D. Li, J. Catal. **229**, 206 (2005)
20. E. Paparazzo, Appl. Catal. B Environ. **105**, 248 (2011)
21. C.R. Li, M.Y. Cui, Q.T. Sun, W.J. Dong, Y.Y. Zheng, K. Tsukamoto, B.Y. Chena, W.H. Tang, J. Alloys Compd. **504**, 498 (2010)
22. G.F. Wang, Q.Y. Mu, T. Chen, Y.D. Wang, J. Alloys Compd. **493**, 202 (2010)
23. W. Gao, Z.Y. Zhang, J. Li, Y.Y. Ma, Y.Q. Qu, Nanoscale **7**, 11686 (2015)
24. F.L. Liang, Y. Yu, W. Zhou, X.Y. Xu, Z.H. Zhu, J. Mater. Chem. A **3**, 634 (2015)
25. A. Younis, D. Chu, Y.V. Kaneti, S. Li, Nanoscale **8**, 378 (2016)
26. C. Zhang, F.M. Meng, L.N. Wang, Mater. Lett. **119**, 1 (2014)
27. H. Li, A. Petz, H. Yan, J.C. Nie, S. Kunsagi-Mate, J. Phys. Chem. C **115**, 1480 (2011)
28. H.R. Tan, J.P.Y. Tan, C. Boothroyd, T.W. Hansen, Y.L. Foo, M. Lin, J. Phys. Chem. C **116**, 242 (2012)
29. A.C. Cabral, L.S. Cavalcante, R.C. Deus, E. Longo, A.Z. Simões, F. Moura, Ceram. Int. **40**, 4445 (2014)
30. X.D. Li, J.G. Li, D. Huo, Z.M. Xiu, X.D. Sun, J. Phys. Chem. C **113**, 1806 (2009)
31. I. Kosacki, V. Petrovsky, H.U. Anderson, P.J. Colomban, Am. Ceram. Soc. **85**, 2646 (2002)
32. J. Zdravković, B. Simović, A. Golubović, D. Poleti, I. Veljković, M. Šćepanović, G. Branković, Ceram. Int. **41**, 1970 (2015)
33. W.H. Weber, K.C. Hass, J.R. Mabride, Phys. Rev. B **48**, 178 (1993)
34. Y.J. Lee, G.H. He, A.J. Akey, R. Si, M. Flytzani-Stephanopoulos, I.P. Herman, J. Am. Chem. Soc. **133**, 12952 (2011)
35. H.L. Lin, C.Y. Wu, R.K. Chiang, J. Colloid Interface Sci. **341**, 12 (2010)
36. X. Lu, X. Li, F. Chen, C. Ni, Z. Chen, J. Alloys Compd. **476**, 958 (2009)
37. B. Choudhury, A. Choudhury, Mater. Chem. Phys. **131**, 666 (2012)
38. S. Maensiri, C. Masingboon, P. Laokul, W. Jareonboon, V. Promarak, P.L. Anderson, S. Seraphin, Cryst. Growth Des. **7**, 950 (2007)
39. D. Jiang, W.Z. Wang, E. Gao, S.M. Sun, L. Zhang, Chem. Commun. **50**, 2005 (2014)
40. C.W. Sun, H. Li, L.Q. Chen, J. Phys. Chem. Solids **68**, 1785 (2007)
41. C.W. Sun, H. Li, H.R. Zhang, Z.X. Wang, L.Q. Chen, Nanotechnology **16**, 1454 (2005)
42. F. Lu, F.M. Meng, L.N. Wang, Y. Sang, J.J. Luo, Micro Nano Lett. **7**, 624 (2012)
43. S.Y. Chen, Y.H. Lu, T.W. Huang, D.C. Yan, C.L. Dong, J. Phys. Chem. C **114**, 19576 (2010)
44. J.H. Chen, Y.J. Lin, H.C. Chang, Y.H. Chen, L. Horng, C.C. Chang, J. Alloys Compd. **548**, 235 (2013)
45. A. Thurber, K.M. Reddy, V. Shutthanandan, M.H. Engelhard, C. Wang, J. Hays, A. Punnoose, Phys. Rev. B **76**, 165206 (2007)
46. A. Tiwari, V.M. Bhosle, S. Ramachandran, N. Sudhakar, J. Narayan, S. Budak, A. Gupta, Appl. Phys. Lett. **88**, 142511 (2006)
47. P. Slusser, D. Kumar, A. Tiwari, Appl. Phys. Lett. **96**, 142506 (2010)
48. S.Y. Chen, C.H. Tsai, M.Z. Huang, D.C. Yan, T.W. Huang, A. Gloter, C.L. Chen, H.J. Lin, C.T. Chen, C.L. Dong, J. Phys. Chem. C **116**, 8707 (2012)
49. M.I.B. Bernardi, A. Mesquita, F. Beron, K.R. Pirota, A.O. de Zevallos, A.C. Doriguetto, H.B. de Carvalho, Phys. Chem. Chem. Phys. **17**, 3072 (2015)
50. L.N. Wang, F.M. Meng, Mater. Res. Bull. **48**, 3492 (2013)